Classification of Neurons in the Adult Mouse Cochlear Nucleus: Linear Discriminant Analysis

Paul B. Manis[1], Michael R. Kasten[1], Ruili Xie[2]

[1]Department of Otolaryngology/Head and Neck Surgery, The University of North Carolina at Chapel Hill

[2]Department of Otolaryngology, The Ohio State University, Columbus, OH

Text Pages:

Figures: 7

Tables: 1

Corresponding Author:

Paul B. Manis, Ph.D.
Dept. of Otolaryngology/Head and Neck Surgery
The University of North Carolina at Chapel Hill
B027 Marsico Hall
125 Mason Farm Road
Chapel Hill, NC 27599-7070

Tel: 919 843 9318
Email: paul_manis@med.unc.edu

Abstract

The cochlear nucleus (CN) transforms the spike trains of spiral ganglion cells into a new set of sensory representations that are essential for auditory discriminations and perception. These transformations require the coordinated activity of different classes of neurons that are embryologically derived from distinct sets of precursors. Decades of investigation have shown that the neurons of the CN are differentiated by their ion channel expression and intrinsic excitability. In the present study we have used linear discriminant analysis (LDA) to perform an unbiased analysis of measures of the responses of CN neurons to current injections to mathematically separate cells on the basis of both morphology and physiology. Recordings were made from cells in brain slices from CBA mice and a transgenic mouse line, NF107, crossed against the Ai32 line. For each cell, responses to current injections were analyzed for spike rate, spike shape (action potential height, afterhyperpolarization depth, first spike half-width), input resistance, resting membrane potential, membrane time constant, hyperpolarization-activated sag and time constant. Cells were filled with dye for morphological classification, and visually classified according to published accounts. The different morphological classes of cells were separated with the LDA. Ventral cochlear nucleus (VCN) bushy cells, planar multipolar (T-stellate) cells, and radiate multipolar (D-stellate) cells were in separate clusters, and were also separated from all of the neurons from the dorsal cochlear nucleus (DCN). Within the DCN, the pyramidal cells and tuberculoventral cells were largely separated from a distinct clusters of cartwheel cells. DCN cells fell largely within a plane in the first 3 principal axes, whereas VCN cells were in 3 clouds approximately orthogonal to this plane. VCN neurons from the two mouse strains were slightly separated, indicating either a strain dependence or the differences in slice preparation methods. We conclude that cochlear nucleus neurons can be objectively distinguished based on their intrinsic electrical properties, but that such distinctions are still best aided by morphological identification.

Introduction

Neurons of the mammalian cochlear nucleus exhibit a variety of responses to intracellular current injection, reflecting the distinct expression of collections of ion channels amongst different classes. However, even within a class, such as bushy cells, individual cells may express specific conductances at different magnitudes [1–3], leading to diversity in excitability features such as action potential threshold, action potential height, and rheobase. In spite of this variability, cells of a given morphological class appear to possess common properties that have been used to identify cells on the basis of their electrical signatures alone [4–12].

Quantitative methods for identifying cell classes have been explored in the context of the myriad interneuronal populations in cortex [13], within the olfactory bulb [14] and across neuronal populations throughout the brain [15]. These methods rely on systematic measurement of distinct features of intrinsic excitability such as action potential shape, firing rates, passive membrane measures, and responses to hyperpolarization, and have used principal components analysis (PCA), support vector machine model, or stepwise linear regressions. Within the cochlear nucleus, application of an hierarchical clustering analysis to *in vivo* single unit data provided evidence for partial separation of unit response types in the gerbil AVCN [16], although further analysis (using PCA) suggested that there was extensive overlap between cell classes.

Here we apply linear discriminant analysis [17] to the problem of separating cell classes in the cochlear nucleus based on intrinsic excitability. Whereas PCA separates classes

3

86   by finding the axes that maximize the variance within a data set, and does not rely on

87   labels, LDA maximizes the separation between classes, utilizing label (e.g., class)

88   information. We find that LDA is an effective tool for segregating the cell classes based

89   on their excitability, while also suggesting that there is either overlap between the

90   properties of some of the classes, or that they may not be entirely morphologically

91   distinguishable. Such a classification tool should be useful in future studies of the

92   excitability of cochlear nucleus neurons following hearing loss as a way of objectively

93   assessing how the excitability of neurons changes.

94

95   **Materials and Methods**

96   Whole cell tight-seal recordings were made in brain slices from adult CBA (P28-69) and

97   NF107::Ai32 (P31-166) mice. The NF107::Ai32 mice are the F1 cross of the NF107

98   mouse line, originally from the GENSAT Consosrtium [18], and the channel rhodopsin

99   (ChR2) expressing line Ai32 [19], and so are on a mixed CD-1, C57Bl/6J and FVB

100   background. The ChR2 was not activated during these experiments. CBA mice were of

101   either sex, whereas the NF107::AI32 mice were only males, as the Cre driver is carried

102   on the Y chromosome.The data from the CBA mice were taken from a previous series

103   of studies [11,20]. Data from the NF107::Ai32 mice were taken from unpublished work

104   (Kasten, Ropp and Manis, in preparation). The CBA slices were prepared following

105   anesthesia (100 mg/kg ketamine and 10 mg/kg xylazine), and decapitation, with slicing

106   in warm ACSF. The NF107::Ai32 slices were prepared using the same anesthesia

107   followed by transcardial perfusion with an NMDG-based solution [21]. Electrodes

108   contained 126 K-gluconate, 6 KCl, 2 NaCl, 10 HEPES, 0.2 EGTA, 4 Mg-ATP, 0.3 Tris-

4

109   GTP, and 10 Tris-phosphocreatine, with pH adjusted to 7.2 with KOH and recordings

110   were made with a MultiClamp 700B (Molecular Devices) amplifier, low-pass filtered at

111   6kHz, and digitized at 10-20 kHz with 16-bit A-D converters (National Instruments).

112   Stimulus presentation and acquisition were controlled by either a custom Matlab®

113   program or by *acq4* [22]. All animal procedures were approved by the University of

114   North Carolina Institutuional and Animal Care Committee (protocols 12-253, 15-253 and

115   18-160).

116   For each cell, responses to current injections (100-500 msec duration, ranging from -1

117   to 4 nA) were analyzed. Data from either acquisition program were converted to a

118   common format for analysis by Python (V3.6) scripts. Passive measures included input

119   resistance (from the slope of the current-voltage relationship just below rest), resting

120   membrane potential, membrane time constant (measured from responses to small

121   hyperpolarizing current steps that produced 2-10 mV voltage deflections), the

122   magnitude of the hyperpolarization sag [23] and the time constant for the sag measured

123   near -80 mV. Active measures included action potential height (measured from rest to

124   action potential peak), first spike half-width (measured at half the action potential height

125   from rest), afterhyperpolarization depth (measured from rest to the first

126   afterhyperpolarization), an adaptation index measured near firing threshold (see below),

127   the number of rebound spikes after hyperpolarizing steps, the coefficient of variation of

128   interspike intervals, and the slope of the firing rate versus current curve for the first 3

129   current levels above threshold. Cells were filled with dyes (AlexaFluor 488 for CBA

130   mice; tetramethylrhodamine biocytin for the NF107:Ai32 mice) for morphological

131   classification, and visually classified according to published accounts, based on digital

132   images and image stacks collected at low (4X) and high (40-63X) power either during or

133   immediately after each cell was recorded.

134   Adaptation was measured for the lowest two levels of current that elicited spikes as:

$$\frac{-2}{N} \sum_{i=0}^{i=N} \left(\frac{t_i}{t_d} - 0.5 \right)$$

135   Where t_i is the time of the ith spike in the trace, t_d is the trace duration, and N is the

136   number of spikes. This measure ranges from -1 to 1. Neurons that fire regularly without

137   adaptation throughout the trace will have an index of 0. Neurons that fire preferentially

138   only at the onset of the trace will have an index of 1, whereas those that fire near the

139   end of the trace will have an index of -1. Thus, bushy cells will have an index of 1,

140   stellate cells and tuberculoventral cells will usually have an index near 0, and pyramidal

141   cells may have a negative index, depending on the delay to the first spike. Note that this

142   measure depends on the current level that is used relative to the spike threshold, as

143   well as the current duration. The adaptation measured at the threshold current was

144   found to be uninformative in preliminary analyses, and so the only adaptation computed

145   from the next higher current that evoked spikes was used.

146

147   All absolute voltage measurements are corrected for a -11 mV junction potential for the

148   K-gluconate electrodes. All other voltage measurements are differential (action potential

149   height from peak to the minimum of the following AHP) and are independent of the

150   junction potential.

151

6

152   Computed measures were then analyzed using LDA and PCA using standard libraries

153   in Python (scikit-learn v0.20, Python 3.6), and in R (3.5, using the packages DisplayR

154   and flipMultivariates).

155

156

157   **Results**

158

159   The discharge patterns of cochlear nucleus neurons have been reported in a series of

160   studies over the years from multiple laboratories using similar, but not identical

161   recording conditions. Fig 1 shows the intrinsic physiology of example cells from six

162   major morphological classes as recorded in our dataset. Briefly, bushy cells (Fig 1A)

163   fire 1-3 action potentials at the onset of depolarizing current injections, and are silent

164   thereafter [4,5]. At higher current levels, oscillatory membrane responses, which may

165   represent axonally initiated action potentials, are sometimes visible. In response to

166   hyperpolarizing pulses, bushy cells can show a slow sag in membrane potential, and

167   following the hyperpolarizing step can generate an anodal break spike. The planar

168   multipolar cells (Fig 1B) fire regularly in response to depolarizing current injections, and

169   also show a slow sag in response to hyperpolarizing current steps; they can also show

170   anodal break spikes [11,23]. Radiate multipolar cells also fire regularly in response to

171   depolarization, sometimes exhibiting an adapting spike train. They show a rapid sag in

172   response to hyperpolarization, and frequently have anodal break spikes. As noted

173   previously [11], radiate multipolar cells also may fire only at the onset of a weak

174   depolarizing current pulse. Pyramidal (fusiform) cells of the dorsal cochlear nucleus fire

7

175 regularly [9,24,25], and may have a long delay to the first spike or a long first interspike

176 interval [25–27]. In the adult mice studies here, these cells do not show a prominent

177 sag, but do show a rapidly activating rectification in response to hyperpolarizing steps,

178 which is likely generated by Kir channels [28]. Cartwheel cells show mixed single-

179 spiking regular firing and burst firing [7,10]. The tuberculoventral neurons show regular

180 firing, and often have trains of re8ound spikes after hyperpolarization [12,29]. The

181 principal cell database included 18 bushy cells, 31 planar multipolar cells, 32 radiate

182 multipolar cells, 38 pyramidal cells, 12 cartwheel cells, and 31 tuberculoventral cells.

183 Additional cell classes (all from the DCN) had too few cells for effective classification.

184 These included 1 "Type-B" cell [30], 1 chestnut cell [31], 7 giant cells, 2 "horizontal

185 bipolar" cells (small neurons in the pyramidal cell layer of the DCN with a bipolar

186 morphology where the moderately spiny dendrites reside mainly within the pyramidal

187 cell layer), 2 molecular layer stellate cells [32], 3 unipolar brush cells [31,33], and 3 cells

188 that could not clearly be identified on comparison with the literature. These were not

189 included in the analyses.

190

191 **Fig 1. Examples of discharge patterns and passive responses, for different levels**

192 **of current injection for 6 classes of cochlear nucleus neurons.** A. Bushy; B. planar

193 multipolar; C. radiate multipolar; D. pyramidal; E. cartwheel; F. tuberculoventral.. Red

194 dots indicate spikes evoked by current injection.

195

196 In order to classify the principal cell types, we extracted a set of measurements from the

197 current-voltage and spiking responses (N = 162 cells). These are illustrated in Figs 2

198   and 3. Fig 2 summarize the passive properties of the cells (columns) against the cell

199   types (rows). From this, differences in the resting membrane potential, input resistances

200   and time constants can be appreciated between the groups. In addition, measurements

201   of the time constant of the hyperpolarizing sag, and a previously-used measure [23], the

202   B/A sag ratio, also show clear differences between the cells, with neurons from the DCN

203   generally showing weaker I_h.

204

205   **Fig 2. Summary of passive measurements from responses to hyperpolarizing**

206   **current pulses across the population of CN neurons.** RMP: resting membrane

207   potential; R_{in}: input resistance; τ_m: membrane time constant; τ_h: time constant of

208   repolarizing sag from traces near -80 mV; B/A: steady-state over peak voltage

209   deflection for hyperpolarizing sag (from Fujino and Oertel, 2001). The ordinate indicates

210   the population density based on the kernel density estimate (blue line). The histograms

211   shows the distribution of values from the population cells for each type and measure.

212

213   Fig 3 shows measures of action potential shape and firing properties. Again, population-

214   based distinctions are evident, such as the relatively small and wide action potentials of

215   bushy cells, and the tendency of tuberculoventral and some cartwheel cells to show

216   rebound responses, and the wide coefficient of variation of firing of the cartwheel cells.

217   The firing rate slope measured near threshold also was lowest for bushy, pyramidal and

218   cartwheel cells, and highest for the planar and radiate multipolar cells, and

219   tuberculoventral cells.

220

9

221 **Fig 3. Summary of action potential shape and firing patterns across the**

222 **population of CN neurons.** AP Peak: action potential peak potential; APHW: action

223 potential half-width; AHP: action potential afterhyperpolarization; Adaptation: adaptation

224 calculated from the response to a suprathreshold current injection; Rebound: count of

225 rebound action potential after the end of the hyperpolarizing current injection; CV:

226 coefficient of variation of interspike intervals; Irate: slope of the current-firing relationship

227 for current levels just above spike threshold. The ordinate indicates the population

228 density based on the kernel density estimate (blue line). The histograms show the

229 distribution of values from the population cells for each type and measure.

230

231 Next, we submitted the data to a LDA, using all of the parameters measured in Figs 2

232 and 3. Data were first standardized for each measure before being submitted to the

233 LDA. The standardization rescaled the individual measurements for each measurement

234 type so that it had a zero mean and a unit standard deviation. Fig 4 illustrates the first 3

235 components of the LDA, with each cell colored by its classified type, in 3 views (Fig 4A,

236 B, C). The LDA effectively separated the different types of cells into distinct spaces. The

237 bushy and cartwheel cells were the most separated from the remainder of the regular

238 firing cells. Interestingly these two cell groups did not form tight clusters, suggesting

239 some diversity in their properties. The pyramidal and tuberculoventral cells were

240 clustered next to each other, although with minimal overlap. The radiate and planar

241 multipolar cells formed two slightly overlapping clusters that were largely separate from

242 all other cell classes. Note that although most of the bushy, planar and radiate

243 multipolar cells were recorded in CBA mice, those cells recorded from the NF107::Ai32

10

244 mice (FVB and C57Bl/6 backgrounds; solid symbols) were close to the measures of the

245 CBA populations, although they were slightly separated in one of the first 3 axes, as

246 more clearly seen in Fig 4D, where only cells from the VCN are shown. Cross-validation

247 of the LDA yielded an estimated accuracy of 0.79 (+/- 0.31).

248

249 **Fig 4. LDA with supervised clustering by cell morphology.** A. The first 3 (largest)

250 LDA components are shown in a perspective view. The axes represent the projections

251 of each cell on to the 3 largest components from the standardized data (zero mean, unit

252 standard deviation; therefore there are no units). Note the clear separation of the bushy

253 cell and cartwheel cells populations from the rest of the CN neurons. Although the other

254 populations are close together, they are also separated as can be appreciated by

255 comparing the different views. Cells from CBA mice are shown with open symbols; cells

256 from the NF107 mice are shown with closed symbols. B, C. Two other perspective

257 views (rotated) of the same data as in A. D. A view of the data for the VCN cells only

258 (bushy, planar multipolar and radiate multipolar) for clarity. This is the same perspective

259 view as panel C.

260

261 We also submitted the data set to a standard principal components analysis, following

262 the same standardization across cells for each measure (Fig 5). In this case, the

263 supervisory classifier (cell morphology) was not used in the initial classification. The

264 PCA resulted in clusters of cells from the same morphological class, but these had

265 greater overlap than with the LDA. Cross-validation of the PCA data yielded a low

266 accuracy of 0.17 (+/- 0.086).

11

267

268   **Fig 5. Principal components analysis (PCA) on the same data set as Fig 4.** The

269   PCA method is not supervised by cell type, and so the results depend only on factors

270   that maximize the variance. The PCA successfully separated the cell classes, but did

271   not have good accuracy with cross-validation. The view shown is the same format as

272   Fig 4A.

273

274   In order to determine which measures provided the most information in the LDA

275   classification, we performed the LDA using combinations of measures, from individual

276   measures through all available measures, and estimated the accuracy of the

277   classification across all cells by dividing the data into training and testing sets. The

278   accuracy as a function of the number of combined measures is shown in Fig 6. As

279   expected, the accuracy improves as new measures are added, up until about 6

280   parameters, at which point the accuracy plateaus. However, the overall *worst* accuracy

281   continues to improve as more measures are added. The black line indicates the mean

282   of the best 5 combinations of measures. From this we conclude that some of the

283   measures are possibly redundant and that some measures may be non-informative.

284   With 7 or 8 combined measures (where the largest number of combinations was

285   tested), AP height, R_{in}, RMP, τ_h and I_{rate} occurred together in each of the 5 most

286   accurate runs. Similar, but not identical distributions were present for 8 combined

287   measures. Note that the accuracy of each point includes a standard deviation estimate

288   (not shown) as it is the result of multiple runs with different subsamples of training and

289   test cells, so the best measures can vary with an arbitrary threshold, and there is no

12

290   single "optimal" set. With the number of cells in the sample and the large number of

291   parameters, the SD can be 15-20% of the mean value.

292

293   **Fig 6. Accuracy of separation for different number of combined measures, using**

294   **the LDA separation score for each set of measures**. All 12 measures were

295   considered in all possible combinations in groups from 1 to 12 (the number of

296   combinations are shown above the data), and each combination is plotted as a point

297   along the ordinate representing the number of combinations. The mean score is

298   indicated by the red line. The average of the best 5 scores for each combination set are

299   plotted as a black line. In general, including more measures improves the accuracy of

300   the separation of groups.

301

302   To further investigate those factors that drove the prediction accuracy, we performed

303   the same analysis using the R package flipMultivariates. Table 1 summarizes the

304   prediction accuracy by cell type, and provides mean measures for each of the

305   parameters. Although all parameters provide a significant contribution (r^2) to the

306   separation, the five that accounted for the largest proportions of the variance ($r^2 > 0.50$)

307   were the AP height, AP half width, the adaptation measure, the coefficient of variation of

308   interspike intervals, and the firing rate slope (I_{rate}). However, all of the measures showed

309   a significant contribution.

310

311

312 **Table 1**

Measure	Bushy	Cartwheel	Radiate Multipolar	Pyramidal	Planar multipolar	Tuberculo-ventral	R^2	p
RMP (mV)	-62.5	-75.2	-63.1	-68.5	-62.7	-67.9	0.41	<0.001
τ_m (ms)	1.29	5.25	2.83	8.04	4.90	12.71	0.41	<0.001
R_{in} (MΩ)	27.5	79.6	60.1	68.8	87.9	155.6	0.39	<0.001
τ_h (ms)	27.5	56.9	12.1	51.0	40.0	74.4	0.32	<0.001
B/A	0.50	0.95	0.39	0.59	0.63	0.71	0.28	<0.001
AP Height (mV)	**-27.6**	**2.9**	**5.9**	**2.2**	**6.7**	**-6.9**	0.63	<0.001
AP Width (ms)	**1.32**	**0.83**	**0.28**	**0.40**	**0.26**	**0.35**	0.73	<0.001
AP AHP (mV)	-57.7	-53.8	-68.3	-64.6	-69.2	-62.1	0.31	<0.001
AP Adaptation	**0.96**	**0.22**	**0.21**	**0.10**	**0.05**	**0.13**	0.62	<0.001
AP Rebound (N)	0.33	1.37	1.17	1.37	1.10	11.41	0.26	<0.001
CV	**N/A**	**0.71**	**0.07**	**0.10**	**0.05**	**0.14**	0.65	<0.001
I_{rate} (spikes/nA)	**5.8**	**768**	**1158**	**412**	**1232**	**1148**	0.51	<0.001
Correct Predictions (%)	94.4	83.3	81.3	92.1	83.9	90.3		

313

314 **Table 1.** Relations between the predictors and each cell class, indicating the number of

315 correct predictions overall, and for each class. The top predicting variabiles (largest R^2

316 values) are highlighted in bold. N = 162 cases used in estimation. Null hypotheses: two-

317 sided; multiple comparisons correction: False Discovery Rate correction applied

318 simultaneously to entire table. N/A: not applicable. See Methods and Materials for

319 details of measurements.

320

321 Fig 7 plots the overall prediction accuracy against the observed classifiers. Although the

322 overall accuracy was fairly high (87.1%), there were several confounds. The most

14

323   common of these was radiate vs. planar multipolar, which occurred in about 25% of the

324   cells in these groups. The next most common confound was misclassifying planar

325   multipolar and tuberculoventral cells as pyramidal cells, followed by pyramidal cells

326   being misclassified as tuberculoventral and planar multipolar cells. As these cells all fire

327   regularly, and have similar measures on other properties, this is not surprising.

328

329   **Fig 7. Prediction accuracy table (confusion matrix) by cell type.** The most frequent

330   mis-classifications occurred amongst cells with similar general firing patterns, such as

331   planar and radiate multipolar cells, and pyramidal and tuberculoventral cells. This table

332   was generated in R using data from all 12 measures. The numbers in each box indicate

333   the proportion of correct classifications for each cell type.

334

335

336   **Discussion**

337

338   We find that cells thoughout the cochlear nucleus can be classified by firing patterns,

339   action potential shapes, and responses to hyperpolarizing steps, as well as their

340   morphology. Although not surprising given the long history of the identification of various

341   electrophysiological features as identifying characteristics of different morphological cell

342   classes, the extension of these comparisons across classes that fire regularly, and the

343   consistency of these measures in a population of cells taken from adult mice extends

344   the previous observations made in younger mice. In addition, these results suggest that

15

345   cells can be reasonably classified, at least coarsely, according to their

346   electrophysiological signatures.

347

348   We found that the linear discriminant analysis can be used to classify cells based on 12

349   measured electrophysiological parameters with ~80% success, although there was little

350   improvement when using more than 7 parameters. This requires that the LDA

351   coefficients be estimated from a standardized (training) set of cells before application to

352   an unidentified population. The selection of the training cell, and the quality of that data

353   set, is critical to the success of the technique. Cell morphology should be positively

354   identified, and ambiguous cases discarded, although it is essential to include a full

355   range of cell properties in each class. The measurements should be complete and

356   precise for each cell. Our data set has three limitations in part because it was collected

357   as part of a different experiments. The first is that due to different levels of

358   hyperpolarizing current injection, the voltages reached with hyperpolarizing pulses were

359   not consistent across cells, so that the estimates of the magnitude of the

360   hyperpolarizing sag are influenced by the variability of the voltages reached. The

361   second is that for depolarizing pulses, not all cells reached saturation of their firing

362   rates. For this reason, we did not include maximal firing rates as a measure, but rather

363   focused on the discharge patterns closer to spike threshold. A third limitation is that the

364   current steps near spike threshold were, in some cells, too coarse to precisely define a

365   threshold current. These limitations partly reflect the different input resistances of

366   neurons, as an example, hyperpolarizing pulses strong enough to damage

367   tuberculoventral cells often fail to hyperpolarize pyramidal cells to -80 mV.

16

368

369 Classification errors principally occurred between cell classes with similar firing patterns,

370 such as planar and radiate multipolar cells, and between pyramidal and tuberculoventral

371 cells. In addition, the TV and bushy cells show significant dispersion in the first 3

372 dimensions of the LDA. This may indicate variability in the intrinsic excitability of these

373 cell classes as noted before [12,34,35], or possibly the existence of distinct subclasses.

374 This dispersion was also evident in the unsupervised PCA analysis. Substantially larger

375 datasets of identified cells from individual strains would be needed to clarify the

376 existence of such subclasses in the electrophysiology. An improvement in the

377 classification would be expected to result from the inclusion of additional parameters

378 such as maximal firing rates and the time courses of synaptic events. In addition, in our

379 data set there was some overlap between the planar and radiate multipolar cells. This

380 may in part reflect the limitations of classification for these two similarly firing cell types,

381 but may also indicate the limitations of our morphological classification method, which

382 was qualitative and relied on fluorescent images of the cells collected during the

383 experiments. The qualitative morphological classification of DCN neurons is much

384 easier, so the overlap between the pyramidal and tuberculoventral cells probably

385 represents the limitations of the measurement parameters used, although it could also

386 reflect a true confluence of intrinsic excitability.

387

388 Part of the dispersion in the VCN cell classes may reflect strain or preparation

389 differences, as the cells from CBA mice were slightly offset from those from the

390 NF107::Ai32 mice along the second LDA component. The strain difference is

17

391   reminiscent of the differences in HCN channels seen in bushy, planar multipolar and

392   octopus cells between ICR and a knockout on a hybrid 129S and C57Bl/6 background

393   [3]. This raises a cautionary flag that the LDA should be trained on data acquired from

394   cells recorded from animals of the same genetic background (and age and preparation

395   techniques) if it is to be used to categorize cells from a novel data set.

396

397   **Acknowledgements**

References

1. Rothman JS, Manis PB. Differential expression of three distinct potassium currents in the ventral cochlear nucleus. J Neurophysiol. 2003;89: 3070–3082. doi:10.1152/jn.00125.2002

2. Rothman JS, Manis PB. The roles potassium currents play in regulating the electrical activity of ventral cochlear nucleus neurons. J Neurophysiol. 2003;89: 3097–3113. doi:10.1152/jn.00127.2002

3. Cao X-J, Oertel D. The magnitudes of hyperpolarization-activated (Ih) and low-voltage-activated potassium (IKL) currents co-vary in neurons of the ventral cochlear nucleus. J Neurophysiol. 2011;106: 630–640. doi:10.1152/jn.00015.2010

4. Oertel D. Synaptic responses and electrical properties of cells in brain slices of the mouse anteroventral cochlear nucleus. J Neurosci. 1983;3: 2043–2053. doi:10.1523/JNEUROSCI.03-10-02043.1983

5. Wu SH, Oertel D. Intracellular injection with horseradish peroxidase of physiologically characterized stellate and bushy cells in slices of mouse anteroventral cochlear nucleus. J Neurosci. 1984;4: 1577–1588. doi:10.1523/JNEUROSCI.04-06-01577.1984

6. Oertel D, Wu SH, Garb MW, Dizack C. Morphology and physiology of cells in slice preparations of the posteroventral cochlear nucleus of mice. J Comp Neurol. 1990;295: 136–154. doi:10.1002/cne.902950112

7. Zhang S, Oertel D. Cartwheel and superficial stellate cells of the dorsal cochlear nucleus of mice: intracellular recordings in slices. J Neurophysiol. 1993;69: 1384–1397. doi:10.1152/jn.1993.69.5.1384
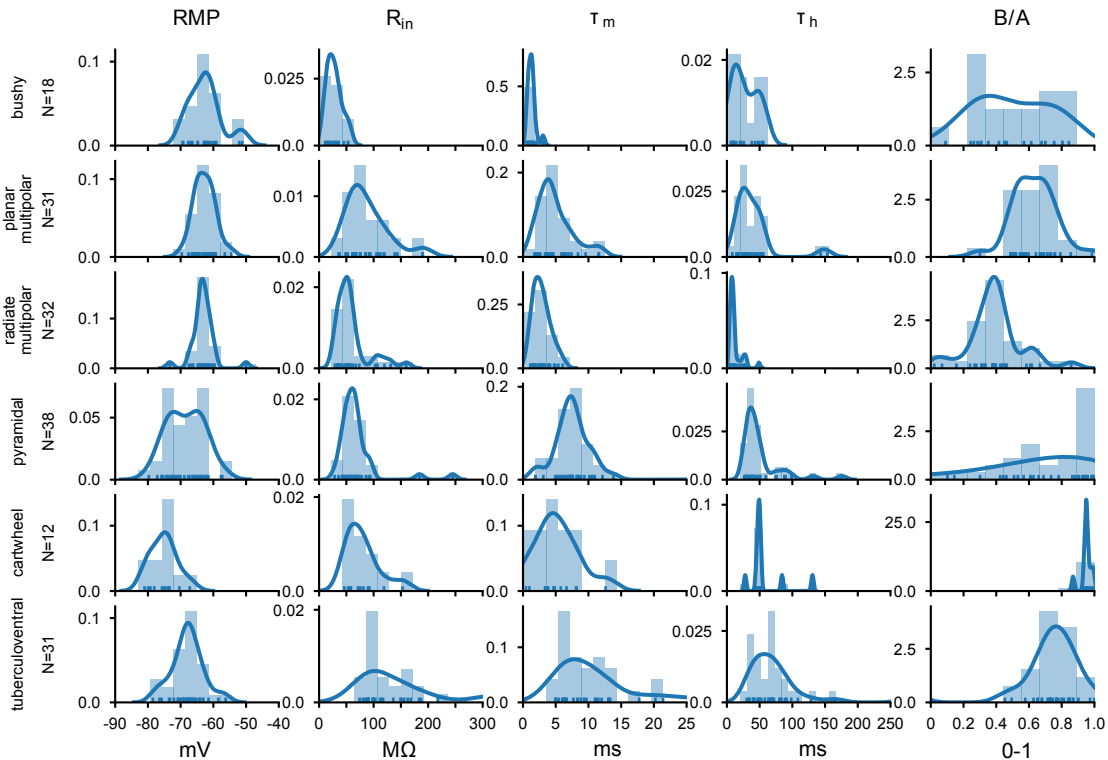
19

425   8.   Zhang S, Oertel D. Giant cells of the dorsal cochlear nucleus of mice: intracellular

426   recordings in slices. J Neurophysiol. 1993;69: 1384–1397.

427   doi:10.1152/jn.1993.69.5.1398

428   9.   Zhang S, Oertel D. Neuronal circuits associated with the output of the dorsal

429   cochlear nucleus through fusiform cells. J Neurophysiol. 1994;71: 914–930.

430   doi:10.1152/jn.1994.71.3.914

431   10.   Manis PB, Spirou GA, Wright DD, Paydar S, Ryugo DK. Physiology and

432   morphology of complex spiking neurons in the guinea pig dorsal cochlear nucleus.

433   J Comp Neurol. 1994;348: 261–276. doi:10.1002/cne.903480208

434   11.   Xie R, Manis PB. Radiate and Planar Multipolar Neurons of the Mouse

435   Anteroventral Cochlear Nucleus: Intrinsic Excitability and Characterization of their

436   Auditory Nerve Input. Front Neural Circuits. 2017;11: 77.

437   doi:10.3389/fncir.2017.00077

438   12.   Kuo SP, Lu H-W, Trussell LO. Intrinsic and synaptic properties of vertical cells of

439   the mouse dorsal cochlear nucleus. J Neurophysiol. 2012;108: 1186–1198.

440   doi:10.1152/jn.00778.2011

441   13.   Druckmann S, Hill S, Schurmann F, Markram H, Segev I. A hierarchical structure

442   of cortical interneuron electrical diversity revealed by automated statistical

443   analysis. Cereb Cortex. 2012/09/20. 2013;23: 2994–3006.

444   doi:10.1093/cercor/bhs290

445   14.   Tavakoli A, Schmaltz A, Schwarz D, Margrie TW, Schaefer AT, Kollo M.

446   Quantitative Association of Anatomical and Functional Classes of Olfactory Bulb

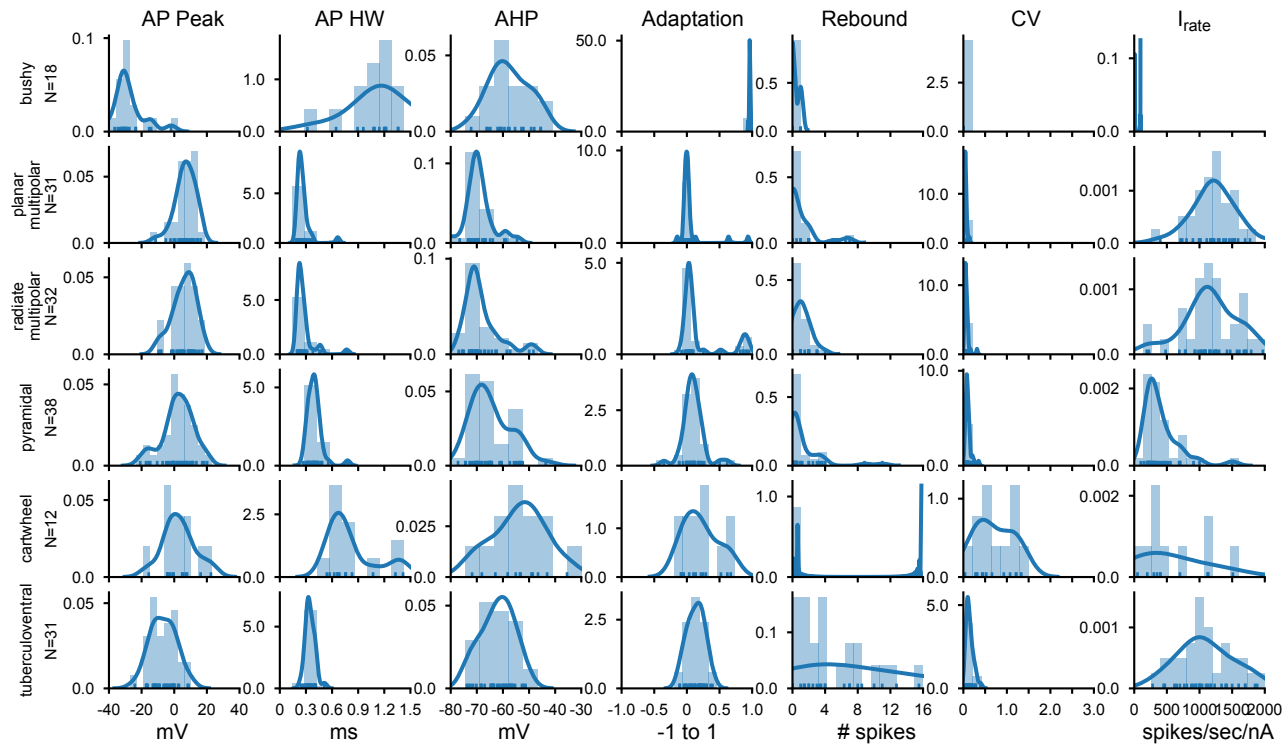447   Neurons. J Neurosci. 2018;38: 7204–7220. doi:10.1523/JNEUROSCI.0303-

448   18.2018

449   15.   Tripathy SJ, Burton SD, Geramita M, Gerkin RC, Urban NN. Brain-wide analysis

450   of electrophysiological diversity yields novel categorization of mammalian neuron

451   types. J Neurophysiol. 2015;113: 3474–3489. doi:10.1152/jn.00237.2015

452   16.   Typlt M, Englitz B, Sonntag M, Dehmel S, Kopp-Scheinpflug C, Ruebsamen R.

453   Multidimensional characterization and differentiation of neurons in the

454   anteroventral cochlear nucleus. PLoS One. 2012;7: e29965.

455   doi:10.1371/journal.pone.0029965

456   17.   Rao CR. The Utilization of Multiple Measurements in Problems of Biological

457   Classification. J R Stat Soc Ser B. 1948;10: 159–203. doi:10.2307/2983775

458   18.   Gong S, Zheng C, Doughty ML, Losos K, Didkovsky N, Schambra UB, et al. A

459   gene expression atlas of the central nervous system based on bacterial artificial

460   chromosomes. Nature. 2003;425: 917–925. doi:10.1038/nature02033

461   19.   Madisen L, Mao T, Koch H, Zhuo J, Berenyi A, Fujisawa S, et al. A toolbox of Cre-

462   dependent optogenetic transgenic mice for light-induced activation and silencing.

463   Nat Neurosci. 2012;15: 793–802. doi:10.1038/nn.3078

464   20.   Xie R, Manis PB. Target-Specific IPSC Kinetics Promote Temporal Processing in

465   Auditory Parallel Pathways. J Neurosci. 2013;33: 1598–1614.

466   doi:10.1523/JNEUROSCI.2541-12.2013

467   21.   Ting JT, Daigle TL, Chen Q, Feng G. Acute Brain Slice Methods for Adult and

468   Aging Animals: Application of Targeted Patch Clamp Analysis and Optogenetics.

469   Methods Mol Biol. 2014;1183: 221–242. doi:10.1007/978-1-4939-1096-0_14

470   22.   Campagnola L, Kratz MB, Manis PB. ACQ4: an open-source software platform for

21

471   data acquisition and analysis in neurophysiology research. Front Neuroinform.

472   2014;8: 3. doi:10.3389/fninf.2014.00003

473 23. Fujino K, Oertel D. Cholinergic modulation of stellate cells in the mammalian

474   ventral cochlear nucleus. J Neurosci. 2001;21: 7372–7383.

475   doi:10.1523/JNEUROSCI.21-18-07372.2001

476 24. Hirsch JA, Oertel D. Intrinsic properties of neurones in the dorsal cochlear

477   nucleus of mice, in vitro. J Physiol. 1988;396: 535–548.

478   doi:10.1113/jphysiol.1988.sp016976

479 25. Manis PB. Membrane properties and discharge characteristics of guinea pig

480   dorsal cochlear nucleus neurons studied in vitro. J Neurosci. 1990;10: 2338–

481   2351. doi:10.1523/JNEUROSCI.10-07-02338.1990

482 26. Kanold PO, Manis PB. Transient potassium currents regulate the discharge

483   patterns of dorsal cochlear nucleus pyramidal cells. J Neurosci. 1999;19: 2195–

484   2208. doi:10.1523/JNEUROSCI.19-06-02195.1999

485 27. Street SE, Manis PB. Action potential timing precision in dorsal cochlear nucleus

486   pyramidal cells. J Neurophysiol. 2007;97: 4162–4172. doi:10.1152/jn.00469.2006

487 28. Leao RM, Li S, Doiron B, Tzounopoulos T. Diverse levels of an inwardly rectifying

488   potassium conductance generate heterogeneous neuronal behavior in a

489   population of dorsal cochlear nucleus pyramidal neurons. J Neurophysiol.

490   2012/03/02. 2012;107: 3008–3019. doi:10.1152/jn.00660.2011

491 29. Zhang S, Oertel D. Tuberculoventral cells of the dorsal cochlear nucleus of mice:

492   intracellular recordings in slices. J Neurophysiol. 1993;69: 1409–1421.
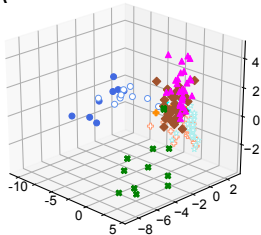
493   doi:8389823

494   30.   Lorente de No R. The Primary Acoustic Nuclei. NY: Raven Press; 1981.

495   31.   Weedman DL, Pongstaporn T, Ryugo DK. Ultrastructural study of the granule cell

496   domain of the cochlear nucleus in rats: mossy fiber endings and their targets. J

497   Comp Neurol. 1996;369: 345–360. doi:10.1002/(SICI)1096-

498   9861(19960603)369:3<345::AID-CNE2>3.0.CO;2-5

499   32.   Apostolides PF, Trussell LO. Superficial stellate cells of the dorsal cochlear

500   nucleus. Front Neural Circuits. 2014;8: 1–9. doi:10.3389/fncir.2014.00063

501   33.   Mugnaini E, Sekerková G, Martina M. The unipolar brush cell: A remarkable

502   neuron finally receiving deserved attention. Brain Res Rev. 2011;66: 220–245.

503   doi:10.1016/j.brainresrev.2010.10.001

504   34.   Francis HW, Manis PB. Effects of deafferentation on the electrophysiology of

505   ventral cochlear nucleus neurons. Hear Res. 2000;149: 91–105.

506   doi:10.1016/S0378-5955(00)00165-9

507   35.   Cao X-J, Shatadal S, Oertel D. Voltage-sensitive conductances of bushy cells of

508   the Mammalian ventral cochlear nucleus. J Neurophysiol. 2007;97: 3961–3975.
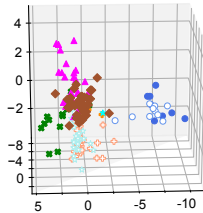
509   doi:10.1152/jn.00052.2007
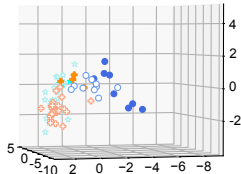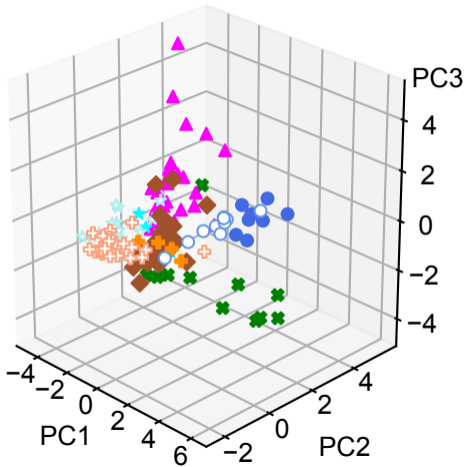
510

A **bushy**
25 mV
25 ms
2017.05.17.s1c0

B **planar multipolar**
25 mV
25 ms
2018.01.26.s0c0

C **radiate multipolar**
25 mV
25 ms
2018.01.26.s0c1

D **pyramidal**
25 mV
25 ms
2018.06.11.s0c0

E **cartwheel**
25 mV
25 ms
2017.11.28.s0c1

F **tuberculoventral**
25 mV
25 ms
2017.05.22.s1c0

A   B   C   D
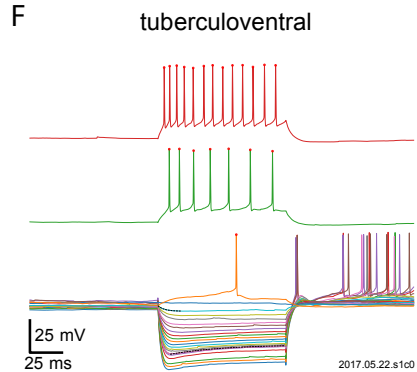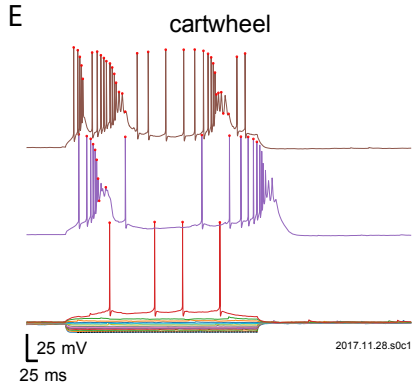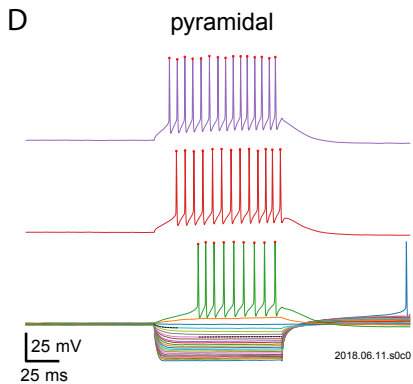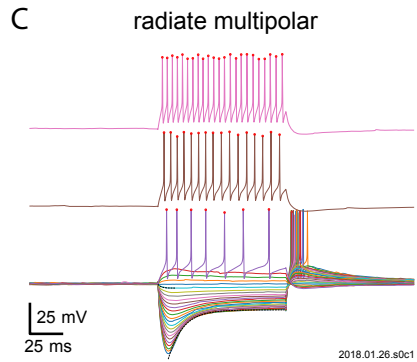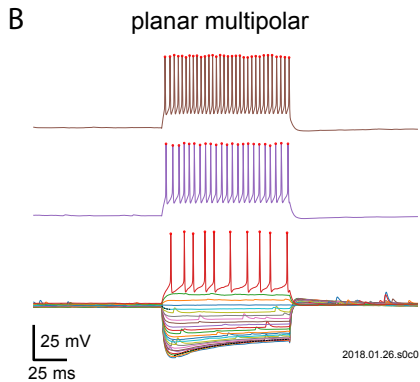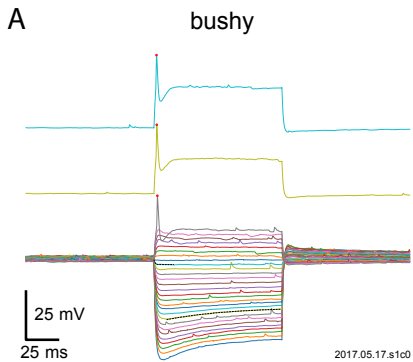
Legend:
- bushy
- planar multipolar
- radiate multipolar
- pyramidal
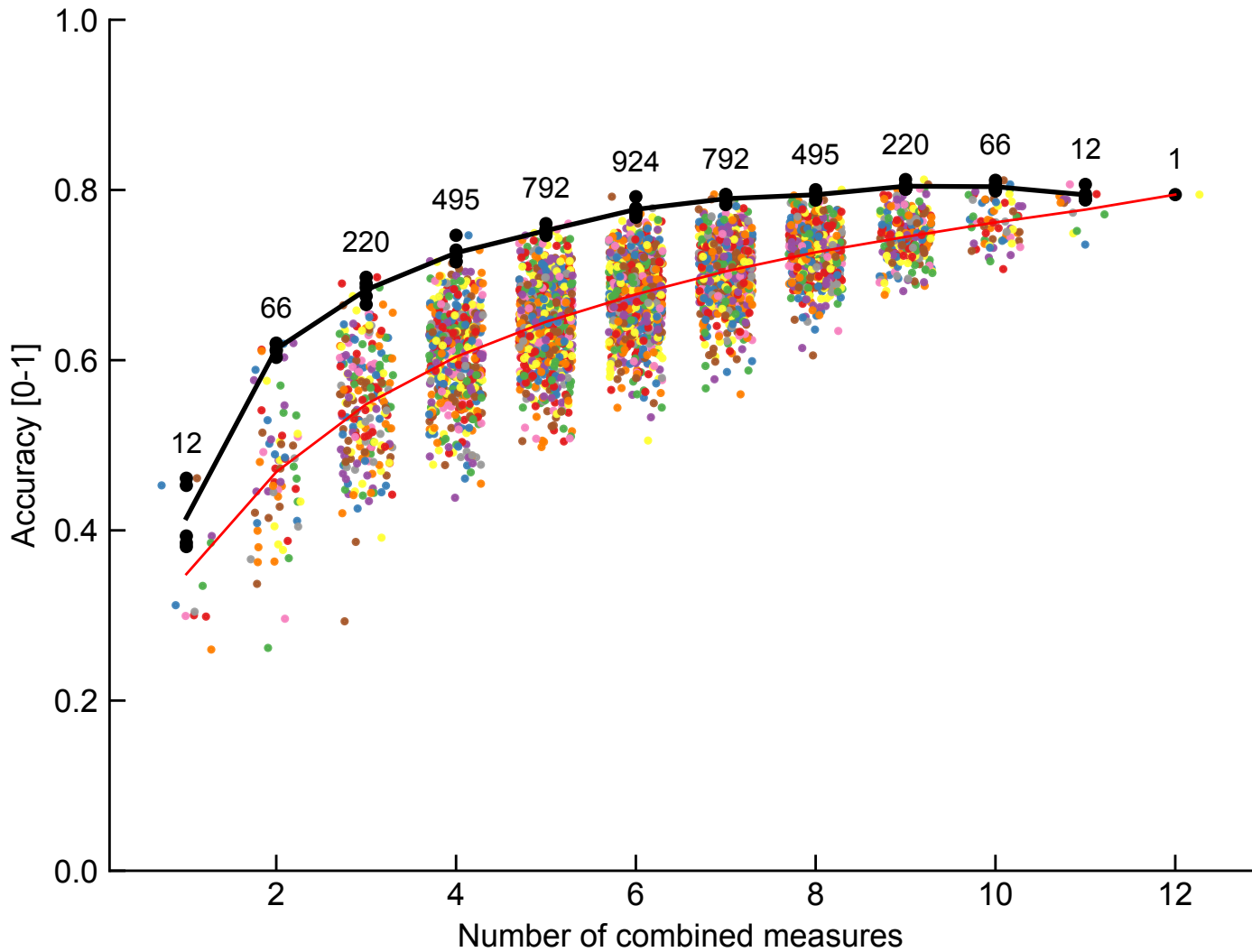- cartwheel
- tuberculoventral

PC3
PC1
PC2
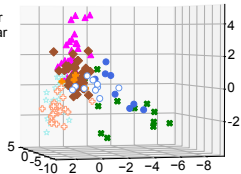
- ● bushy
- ✕ cartwheel
- ✚ radiate multipolar
- ◆ pyramidal
- ✦ planar multipolar
- ▲ tuberculoventral

Confusion matrix